Soft Matter

Microdomains and Stress Distributions in Bacterial Monolayers on Curved Interfaces

Journal:	*Soft Matter*
Manuscript ID	SM-ART-11-2022-001498.R2
Article Type:	Paper
Date Submitted by the Author:	17-Apr-2023
Complete List of Authors:	Langeslay, Blake; University of Illinois at Urbana-Champaign, Physics Juarez, Gabriel; University of Illinois at Urbana-Champaign,

Microdomains and Stress Distributions in Bacterial Monolayers on Curved Interfaces

Blake Langeslay[1] and Gabriel Juarez[2*]

[1]*Department of Physics, University of Illinois at Urbana-Champaign, Urbana, Illinois 61801, USA and*

[2]*Department of Mechanical Science and Engineering, University of Illinois at Urbana-Champaign, Urbana, Illinois 61801, USA*

(Dated: May 1, 2023)

Abstract

Monolayers of growing non-motile rod-shaped bacteria act as active nematic materials composed of hard particles rather than the flexible components of other commonly studied active nematics. The organization of these granular monolayers has been studied on flat surfaces but not on curved surfaces, which are known to change the behavior of other active nematics. We use molecular dynamics simulations to track alignment and stress in growing monolayers fixed to curved surfaces, and investigate how these vary with changing surface curvature and cell aspect ratio. We find that the length scale of alignment (measured by average microdomain size) increases with cell aspect ratio and decreases with curvature. Additionally, we find that alignment controls the distribution of extensile stresses in the monolayer by concentrating stress in negative-order regions. These results connect active nematic physics to bacterial monolayers and can be applied to model bacteria growing on droplets, such as oil-degrading marine bacteria.

* Email address.; gjuarez@illinois.edu

I. INTRODUCTION

The role of mechanical forces in bacterial growth is of increasing interest to both biologists and physicists [1–6]. Bacteria colonize a wide variety of interfaces (liquid-solid, liquid-air, liquid-liquid) with vastly different properties [7–10]. To thrive under these diverse conditions, cells must contend with physical forces such as surface tension and hydrodynamic interactions to stably adhere to the interface over many generations. Bacteria growing on a flat interface as a monolayer of cells have been successfully modeled as an active nematic material. This is a widely studied class of active liquid crystal whose components align parallel to one another and have end-to-end symmetry [2, 11]. Rod-shaped bacteria cells have the required symmetry and, when in a dense monolayer, align due to steric interactions between cells. Extensile activity can be produced by motility [12] or by the growth and division of the cells [11]. In either case, forces in the monolayer are strongly coupled to alignment, as both motility and growth exert forces along the axis of orientation.

The active nematic model of bacterial monolayers has proven powerful in predicting the internal forces and behavior of real systems such as monolayers of gliding *Myxococcus xanthus* and chaining *Bacillus subtilis* biofilms [12, 13]. In particular, the behavior of cells near topological defects has been successfully tied to the behavior of other well-studied active nematic systems. Topological defects are singularities in the director field of liquid crystal alignment. At these locations, there is a net rotation of the director field, which is used to define the defect's charge. In active nematic materials, defects are almost always limited to charges of $\pm 1/2$ [14]. These singularities drive much of the unique behavior of active nematics. Comet-shaped $+1/2$ defects move as motile particles that generate complex flows [14, 15]. In other systems, material is accumulated at positively charged defects while it is depleted at negatively charged defects, allowing 2D materials to escape into the third dimension by multilayering or buckling [16–20]. This last effect has been observed to drive transitions from monolayers to multilayered 3D structures [12, 13].

Previous work on monolayers of rod-shaped bacteria has indicated that their alignment behavior is dependent on whether the cells are hard rods (such as *E. coli*) or whether they are flexible rods (such as *M. xanthus*) [2, 12, 21]. In this case of hard rods, cells have been observed to segregate into microdomains, regions of near-parallel local alignment analogous to grains in crystalline or granular materials [2]. Rather than having a continuous,

gradually changing alignment field, these systems exhibit sharp changes in alignment across the boundaries between microdomains. This represents a fundamentally different type of liquid crystal behavior from that observed in active nematics composed of microtubules or flexible cells. In these systems, microdomains and their boundaries can replace topological defects as a way of mapping alignment [2].

The alignment behavior of simulated and microtubule-based active nematic materials is well known to change based on the curvature of their substrate. Topological defects respond to curvature, with $+1/2$ ($-1/2$) defects accumulating at regions of positive (negative) Gaussian curvature [22–24]. However, it is currently unknown what effect curvature might have on the alignment of a more granular hard-cell system. One such system is a monolayer of the oil-degrading bacterium *Alcanivorax borkumensis* growing on the surface of an oil droplet in water. These cells have been observed to lie tangent to the oil-water interface and grow to form a single monolayer. After completely covering the available surface area of the oil droplet, the continued growth of cells within the monolayer generates interfacial stresses that lead to the deformation of the oil-water interface [25, 26]. To understand how interfacial growth stresses behave in a curved growing monolayer, it is crucial to first understand the alignment behavior of cells within the layer.

To investigate this issue, we simulated the growth of rod-shaped cells adsorbed tangent to the surface of spherical droplets. This enabled analysis of how substrate curvature influences cell alignment and, therefore, stress within the monolayer. We find that both cell aspect ratio and surface curvature play a role in controlling the length scale of alignment, with higher curvature substrates limiting alignment. Additionally, we find that regions of high stress are predicted by negative orientational order. These results enable predictions of how granular monolayer behavior might vary on differently curved surfaces.

II. METHODS

A. Experiments of bacterial growth at flat liquid interfaces

Cell cultures of *A. borkumensis* were grown for 24 hours in ATCC medium 2698 at 30 °C in an orbital shaker at 180 RPM. Cells were non-motile and rod-shaped with an average length of 2.7 µm and width of 0.7 µm. To observe bacterial growth at oil-water interfaces, a

custom microfluidic device was used. A flat oil-water interface was pinned to a microscope slide by a thin copper TEM grid (18 µm, SPI Supplies, 2010C-XA) with square apertures 205 µm wide. The cell culture was injected above this, allowing cells to adsorb on the interface. Then, a microfluidic chamber was constructed around the grid to house the interface and allow for the constant flow of growth media (diluted 10:1 with artificial seawater) at 2 µL min^{-1}. This flow prevented additional cells from settling on the grid during the experiment.

Time-lapse phase contrast microscopy was used to image the growing cell colony for 8 hours using a 60× objective (NA = 0.6 and a depth of field of 2 µm). A single square aperture in the TEM grid was imaged in an experiment, selected for clarity and lack of visible contaminants. Images were recorded with a 50 ms exposure time at 2-minute intervals for 24 hours (see supplementary video SV1).

B. Simulations of bacterial growth on flat and curved surfaces

Molecular dynamics simulations were conducted to obtain precise quantitative data on the physical characteristics of growing bacterial monolayers on flat and curved liquid-liquid interfaces. Each cell was modeled as a spherocylinder with a diameter d_0 and length l between the endcaps. To simulate cell growth, the length of the cylinder l increased linearly with time up to a maximum length l_0 while the diameter remained fixed at d_0.

To model cells adsorbed on 2D surfaces, the center of volume of cells was constrained to coincide with the surface and the cell orientation was constrained parallel to the surface (or to the tangent plane at the point of contact, for spherical surfaces). Therefore, no out-of-plane motion was allowed. Out-of-plane forces and torques were assumed to be balanced by the surface tension of the interface. The changes in position $\vec{x}$ and orientation θ of each cell were modeled by the overdamped Newton's equations as follows:

$$\frac{d\vec{x}}{dt} = \frac{1}{l\zeta}\vec{F}_{\parallel} \tag{1}$$

$$\frac{d\theta}{dt} = \frac{12}{l^3\zeta}\tau_N \tag{2}$$

where $\vec{F}_{\parallel}$ is the total force on the cell due to cell-cell interactions after projection onto the plane tangent to the sphere at the cell's center. Similarly, τ_N is the torque on the cell projected to be normal to the same plane. Here ζ is a drag per unit length. This

term originates from Stokes drag on the adsorbed cells, thereby justifying the choice of overdamped motion [27].

The interactions between cells were modeled as Hertzian forces, with the force on cell i due to cell j acting at the point of contact and calculated as follows:

$$\vec{F_{ij}} = Y d_0^{1/2} h_{ij}^{3/2} \vec{N_{ij}} \tag{3}$$

where Y is proportional to the Young's modulus of a cell, h_{ij} is the overlap distance between the two cell bodies, and $\vec{N_{ij}}$ is the vector normal to cell j at the point of contact [2, 28, 29]. Additionally, to prevent perfect alignment of cells, each cell was subject to a "noise" force $\vec{\eta}$ at each time step with random components η_x, η_y, η_z each in the range $[-\eta_0, \eta_0]$.

Cell growth was modeled using a time-independent rate g_0. To prevent the synchronized division of cells, each cell was assigned random a value between $g_0/2$ and $3g_0/2$ for the growth rate. Whenever a cell length l exceeded the maximum length l_0, cell division would occur where the cell would split into two identical cells, each with a length $(l_0 - d_0)/2$. The new cell would be initialized with the same orientation θ as the original cell, however, the new cell would be assigned a different randomized growth rate. At each time step, cells with lengths greater than l_0 were divided, then forces and torques on cells were calculated. Finally, cell positions were updated using the explicit Euler method to numerically integrate the equations of motion.

Simulations of growth on flat surfaces were conducted in a square periodic boundary of 40 µm per side. To correspond to experiments, simulations were initialized $22 \leq N \leq 26$ randomly placed and oriented cells. Simulations of growth on spherical surfaces were initialized with two parent cells, one located at the north pole and the other at the south pole of the sphere. This resulted in two hemispherical colonies growing until contact was made at the equator, after which, the distribution of cells rapidly became homogeneous across the entire surface. Data was collected on fully-covered spheres once they had reached a packing fraction of $\phi = 1.05$; where ϕ was defined as the area fraction of the surface covered by cells, $\frac{1}{A_{sphere}} \sum_i a_i$, where a_i is the area of the ith cell projected onto the tangent plane to the sphere's surface at the cell's center.

Simulation model parameter values were chosen to be representative of a generic gram-negative, rod-shaped bacterium, including those for the *A. borkumensis* cells used in experiments at flat liquid interfaces [2]. Therefore, the values were set to the following: cell

diameter d_0 to 0.7 µm, Young's modulus Y to 4 MPa, drag per unit length ζ to 200 Pa h, and growth rate g_0 to 2 µm h^{-1}. A simulation time step of 5×10^{-6} hours was used, with a maximum noise η_0 of 2×10^{-9} N. To study the effect of different cell aspect ratios, the maximum growth length allowed was varied between $2 < l_0 < 5$ µm. Cell elongation was parametrized with the aspect ratio α, defined here as $\alpha = (l_0 + d_0)/d_0$, therefore, ranging from $3.9 < \alpha < 8.1$. To study the effect of varying substrate curvature κ, spherical substrates with radius $R = 10, 12, 15, 20,$ and 30 µm were used. Here, substrate curvature is defined as the Gaussian curvature, or $\kappa = R^{-2}$, for a spherical surface. The surface curvatures and cell lengths here were chosen such that cells following the surface constraint (tangent to the surface and attached at their center) did not extend more than $d_0/2$ above the interface, thus ensuring that they intersected the interface throughout their length.

III. RESULTS

In both experiments and simulations, bacteria grow and divide at the surface, forming a monolayer that eventually covers the entire available surface area, shown in Fig. 1. At early times, single cells grow and divide to form colonies, shown in Fig. 1 (top row). At later times, as the cells continue to grow and divide, their contact forces and torques cause them to align with their neighbors to form a liquid crystal with nematic symmetry, shown in Fig 1 (bottom row). As cells grow, the area covered by the colony increases exponentially with time until the available surface area is fully covered. These behaviors are consistently observed in experiments of growth on flat interfaces and in simulations of growth on flat and spherical substrates (Fig. 1). A side-by-side qualitative comparison of experimental and simulated results with similar color schemes and cell sizes is shown in supplementary information Fig. S1.

To establish correspondence between experiments on liquid-liquid interfaces and simulations, the distribution of topological defects in cell monolayers on flat interfaces and substrates, respectively, are compared. First, to identify topological defects, a director field was established. In experiments, the director field was determined using a custom image-processing algorithm based on the brightness gradient of the phase contrast images (see supplementary information). In simulations, the director field was generated directly from the position and orientation of each cell. Then, to locate topological defects within the di-

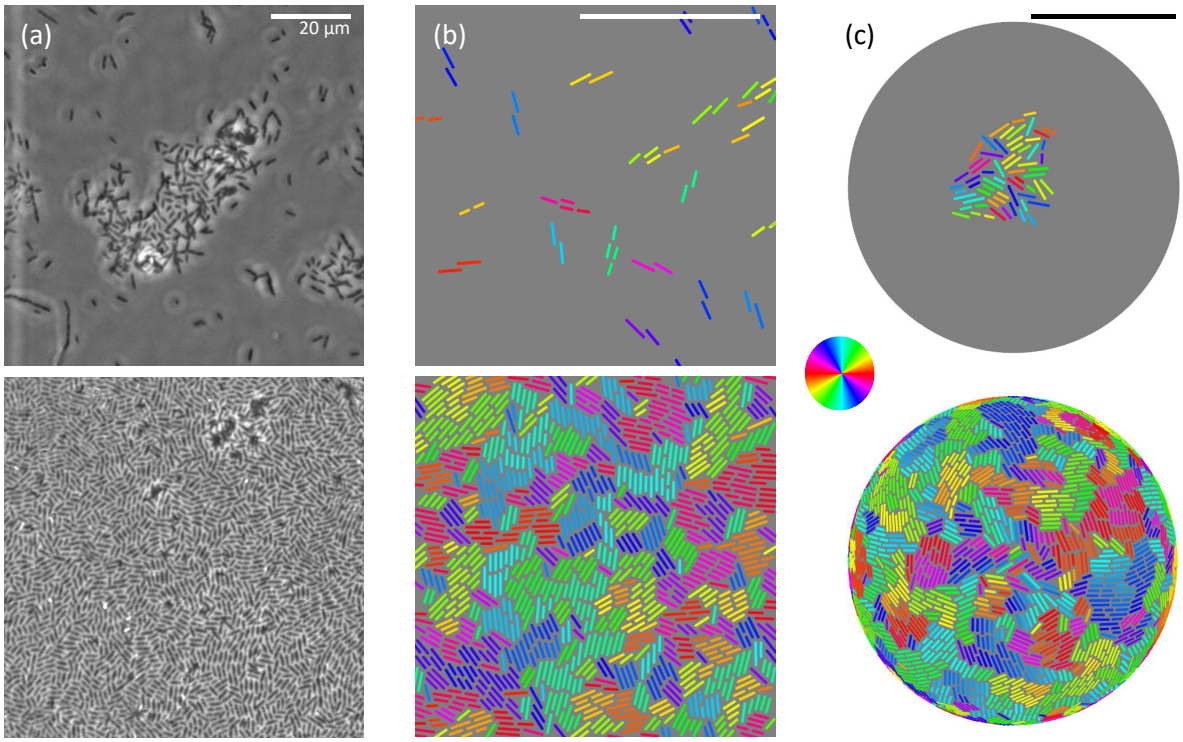

FIG. 1. Formation of a bacterial monolayer due to growth at flat and curved substrates. (a) Micrographs of *A. borkumensis* cells growing on a flat liquid interface at (top) early times and (bottom) up to full surface coverage. (b, c) Simulations of cell growth on (b) flat and (c) spherical substrates with $R = 20$ µm at (top) early times and (bottom) up to full surface coverage. Colors correspond to the cell orientation angle. All scale bars shown represent 20 µm. See supplementary videos SV1, SV2, and SV3.

rector field, each point on the grid (or each cell in simulations) was tested for a net rotation of the surrounding director field (with net rotations of $\pm\pi$ corresponding to defect charges of $\pm 1/2$) [30]. Nearby points with similar net rotations were then grouped by a clustering algorithm with the centroid of each cluster corresponding to a defect of the associated charge.

The distribution of topological defects in experiments at flat interfaces was compared to that in simulations of growing cells with the same dimensions as *A. borkumensis* on flat substrates, shown in Fig. 2 (top row, flat) and supplementary information Fig. S2. To find the length scale of alignment, the average defect separation $\langle \delta x \rangle$ was calculated as $\langle \delta x \rangle = \rho^{-1/2}$, where ρ is the defect density. In each experimental field of view, there were at least

≥ 400 defects. In experiments, the mean defect separation over four experiments is 9.8 ± 0.8 µm. In simulations, the mean defect separation over five simulations is 9.0 ± 0.3 µm. Here, the uncertainties represent the standard error. Based on this qualitative and quantitative agreement between experiments and simulations, the simulation model previously used for liquid-solid interfaces also captures the salient features at liquid-liquid interfaces in the packing fraction regime tested here.

Next, the effect of cell aspect ratio α and substrate curvature κ on orientational order, the degree of alignment, and stress within the cell monolayer was investigated using simulations. First, the orientational order S was evaluated to measure the degree of local alignment in the monolayer. This was calculated at each individual cell i using the following equation:

$$S_i = \frac{1}{N} \sum_j 2\cos^2(\theta_i - \theta_j) - 1 \tag{4}$$

where θ_j is the orientation of each cell whose center lies within a search radius of cell i, N is the total number of cells within the search radius, and the difference in angles is calculated accounting for parallel transport on the curved surface. For the purpose of this analysis, the search radius was set equal to the division length l_0 of the cells. Here, $S \to 1$ represents ordered regions while $S \to 0$ represents disordered regions.

Simulations reveal regions of high order separated by regions of low order, shown in Fig. 2 (top row). These regions of high cell alignment emerge for all combinations of substrate curvature and cell aspect ratio, including flat substrates. For a given curvature, increasing the cell aspect ratio from $\alpha = 4.9$ to $\alpha = 6.7$ increases the size of these regions, shown in Fig. 2 ($R = 20$ µm). Additionally, topological defects tend to coincide with areas of low order, shown in Fig. 2 (top row). This follows from the definition of defects, as the net rotation of the director field around the defect requires imperfect alignment. Therefore, increasing the cell aspect ratio also increases the distance between $\pm 1/2$ defects, as shown in supplementary information Fig. S3.

Next, the mean microdomain area $\langle A \rangle$ was calculated to characterize the degree of cell alignment in the monolayer. Boundaries between microdomains are one-dimensional discontinuities in the alignment field rather than point defects, separating regions of near-parallel alignment. Cells were sorted into microdomains using the following two criteria: two cells must be in the same domain if (i) they were in contact with one another and (ii) their orientation differed by less than 0.2 radians. Each pair of cells was checked to create an adjacency

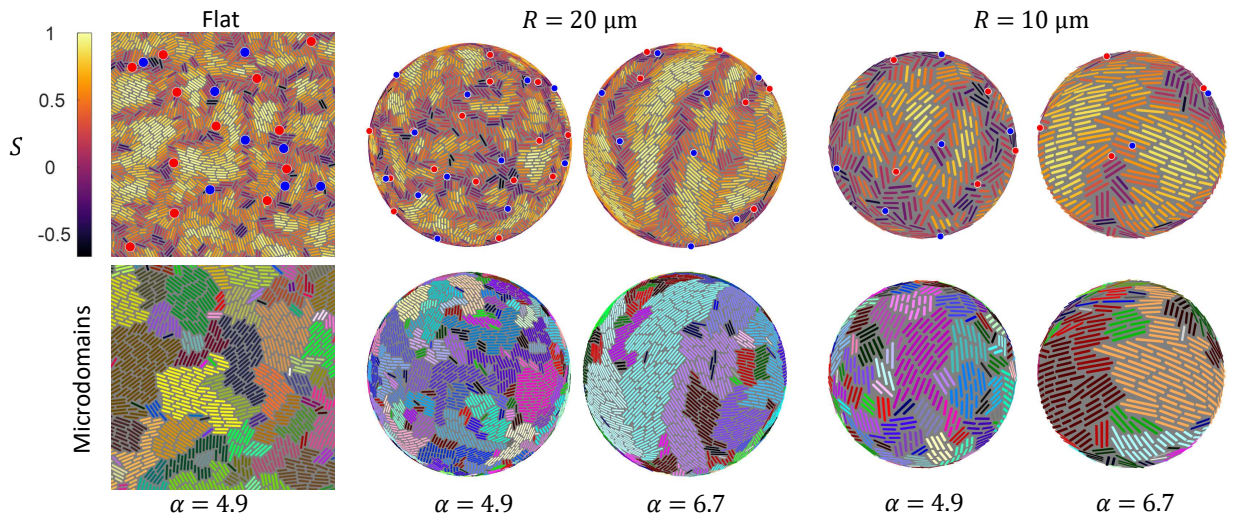

FIG. 2. Orientational order, topological defects, and microdomains in simulations of monolayers with varying cell aspect ratio α and substrate radii R. (Top row) Orientational order S and topological defects with charge $\pm 1/2$ shown in red/blue, respectively. Topological defects tend to occur in regions of low orientational order for all aspect ratios and substrate radii. (Bottom row) Microdomain representation of the cell monolayers shown in the top row. Microdomain boundaries tend to coincide with regions of low orientational order for all aspect ratios and substrate radii. For visualization purposes, spherical substrates ($R = 10$ μm and $R = 20$ μm) are not shown to scale while the field of view for the flat simulations (leftmost column) is 50×50 μm.

matrix, which then produced an unambiguous sorting into distinct microdomains.

Microdomains, represented as differently colored regions, correspond to regions of high-aligned cells, shown in Fig. 2 (bottom row). Borders between large microdomains correspond to regions of low order, reflecting the discontinuity in alignment between microdomains. Similarly, for a given curvature, increasing the cell aspect ratio increases the size of a single microdomain, shown in Fig. 2 ($R = 20$ μm). The area of a microdomain is given as $A = \phi^{-1} \sum a_i$, where a_i are the projected areas of each cell within the microdomain. The distributions of microdomain areas for each aspect ratio and surface curvature are shown in supplementary information Fig. S4. The mean microdomain area for a system is used to characterize the area scale of its cell alignment.

The mean microdomain area increased with increasing cell aspect ratio, shown in Fig. 3(a). For the lowest curvature ($\kappa = 0.001$ μm^{-2}, $R = 30$ μm) the effect of cell aspect ratio

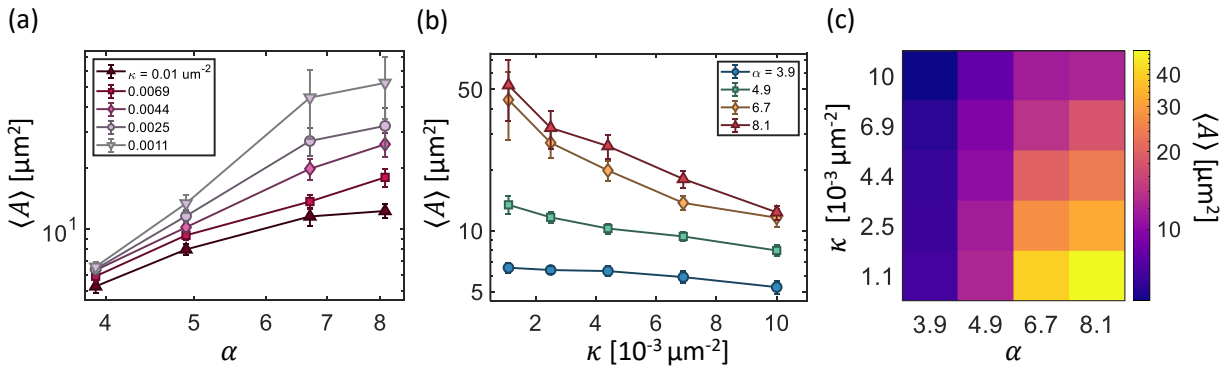

FIG. 3. The effect of cell aspect ratio and substrate curvature on microdomain area. (a) Log-log plot of mean microdomain area $\langle A \rangle$ for different cell aspect ratios α on five different substrate curvatures. Error bars represent standard error. Microdomain area increases with the aspect ratio for all curvatures. (b) Semilog plot of mean microdomain area $\langle A \rangle$ for different substrate curvatures κ and four different cell aspect ratios. Error bars represent standard error. Microdomain area decreases with substrate curvature for all aspect ratios. (c) Summary of the mean microdomain area $\langle A \rangle$ across the simulated parameter space of aspect ratio and substrate curvature.

was the most dramatic, with an increase in the mean domain area of seven-fold. For the highest curvature ($\kappa = 0.01$ μm^{-2}, $R = 10$ μm), however, the effect of cell aspect ratio was less prominent, producing an increase in the domain area of a factor of two. The increase in alignment at higher α is consistent with previous work on bacterial monolayers, which has shown that more elongated (higher aspect ratio) cells produce stronger alignment in flat monolayers [2]. To test that these results are not sensitive to the specific form of cell growth in our model, we conducted a limited set of extra simulations in which doubling time rather than growth rate was held constant. A comparison between results with the two types of growth is shown in supplementary information Fig. S5. The same relation between aspect ratio and microdomain area holds in both cases.

The mean microdomain area decreased with increasing substrate curvature, shown in Fig. 3(b). The effect was more pronounced for higher aspect ratio cells. Simulations with the highest aspect ratio ($\alpha = 8.1$) produced a 75% decrease in microdomain area over the range of curvatures investigated, while simulations with the lowest aspect ratio ($\alpha = 3.9$) exhibited a decrease of only 20%. In all cases, however, more curved substrates produced consistently lower microdomain areas.

Measurements of mean domain area across a range of aspect ratios and curvatures were combined to show the system's response over the $\alpha - \kappa$ parameter space, shown in Fig. 3(c). The combined effect of cell aspect ratio and substrate curvature on microdomain area is evident. The largest domain areas are observed at high cell aspect ratios and low substrate curvatures. The smallest domain areas, however, are observed at low cell aspect ratios and high substrate curvatures.

Lastly, the parallel component of the Virial stress $\sigma_{\parallel}$ on each cell was measured to determine the force distributions in the monolayer. The Virial stress $\boldsymbol{\sigma}_i$ on a cell is given as follows [2, 6]:

$$\boldsymbol{\sigma}_i = \frac{\phi}{a_i} \sum_j \boldsymbol{r}_{ij} \boldsymbol{F}_{ij} \tag{5}$$

where a_i is the area of cell i's projection onto the tangent plane, $\boldsymbol{r}_{ij}$ is the vector from the center of cell i to the point of contact with cell j, and $\boldsymbol{F}_{ij}$ is the force from cell j on cell i. When $\boldsymbol{\sigma}$ is calculated in the basis of vectors parallel and perpendicular to the cell's orientation in the plane tangent to the sphere at the cell's center, it can be decomposed into parallel ($\sigma_{\parallel}$), perpendicular ($\sigma_{\perp}$), and shear (τ) components:

$$\boldsymbol{\sigma} = \begin{bmatrix} \sigma_{\parallel} & \tau_{ij} \\ \tau_{ji} & \sigma_{\perp} \end{bmatrix}$$

The parallel stress $\sigma_{\parallel}$ corresponds to the force in the direction of the cells' growth. Because of the extensile nature of the system, $\sigma_{\parallel}$ and $\sigma_{\perp}$ are always negative (corresponding to a compressive force), while the shear stresses are much lower on average because all forces between cells are normal to the cells' surfaces at the point of contact.

The parallel component of the Virial stress, normalized by the mean stress, for each cell in the monolayer on a curved substrate with $R = 15$ µm is visualized and shown in Fig. 4(a). At the cell level, the normalized stress varied over a wide range of values. For example, for $\alpha = 4.9$ and $R = 15$, the mean stress was $\langle \sigma_{\parallel} \rangle = -0.030$ N/m, and the normalized stress varied from a minimum of zero up to a maximum of $\sim 3.1 \langle \sigma_{\parallel} \rangle$. For an aspect ratio of $\alpha = 6.7$ and the same surface curvature, the mean stress was $\langle \sigma_{\parallel} \rangle = -0.025$ N/m and the normalized stress varied from a minimum of zero up to a maximum of $\sim 4.7 \langle \sigma_{\parallel} \rangle$. Stress visualization in growing monolayers with varying values of α and κ can be seen in supplementary videos SV4 – SV7. The average parallel and perpendicular stress at each aspect ratio and curvature are shown in supplementary information Fig. S6(a,b,d,e).

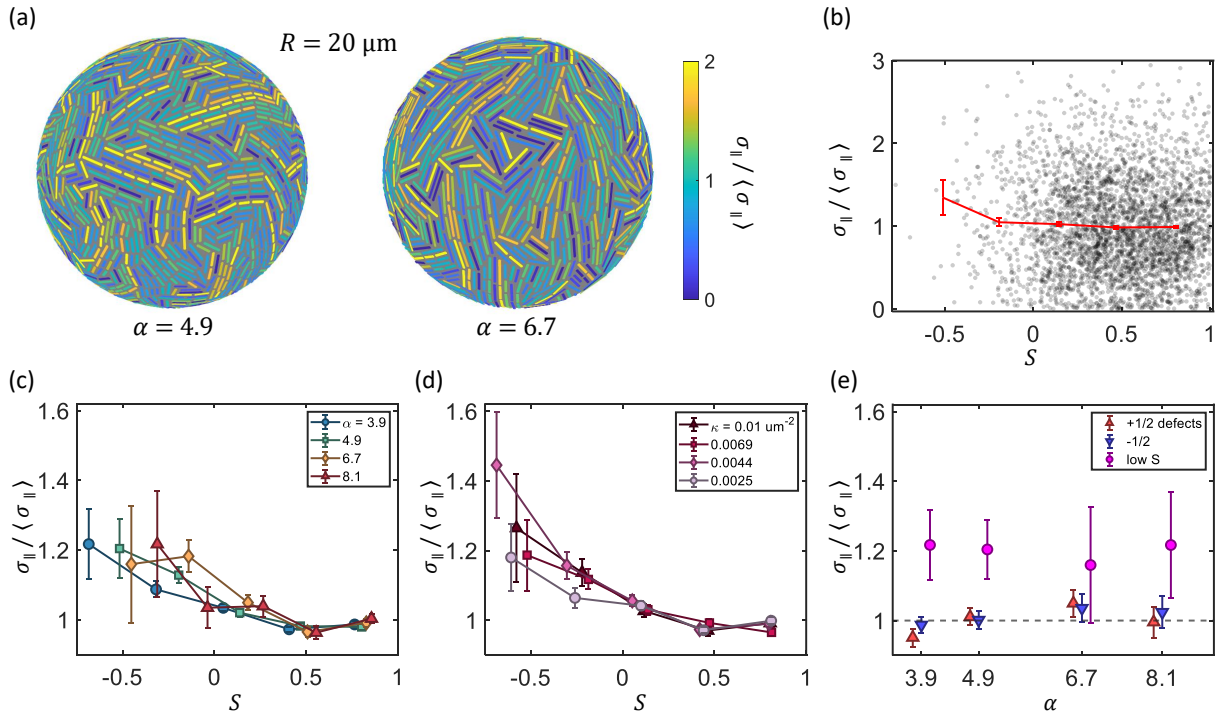

FIG. 4. Parallel component of the Virial stress $\sigma_{\parallel}$ in growing cell monolayers on curved surfaces. (a) Visualization of the normalized parallel stress in cell monolayers on a curved surface with $R = 15$ μm and for cell aspect ratios of $\alpha = 4.9$ and 6.7. (b) Scatter plot of the normalized parallel stress of individual cells and their local orientational order for the case of $R = 20$ μm and $\alpha = 4.9$. The trendline shows the data binned by orientation order. (c) Relation between the normalized parallel stress magnitude and the orientational order for differing aspect ratios. Average parallel stress magnitude increases by up to 20% in the most negative order bin. (d) Relation between the parallel stress magnitude and the orientational order for differing surface curvatures. (e) Deviation from mean parallel stress at topological defects (+1/2 in red, −1/2 in blue) and in the most negative order regions (in magenta). Negative-order regions have a greater deviation from the mean stress than topological defects for all curvatures and aspect ratios. All error bars show standard error.

A scatter plot of the normalized parallel component of Virial stress and the orientational order for a representative simulation ($R = 20$, $\alpha = 4.9$) is shown in Fig. 4(b), grey points. It is evident that, at the individual cell level, stress values can vary over a wide range with respect to the average value of stress. No trend is immediately visible in the scattered data, however, binning the data by the orientational order S reveals a relationship between the

normalized stress $\sigma_{\parallel}/\langle\sigma_{\parallel}\rangle$ and orientational order S. First, five evenly spaced bins were determined by identifying the minimum S_{min} and maximum S_{max} values of the orientational order for each simulation. Then, the mean orientational order and mean parallel stress were computed for each bin. The result is shown in Fig. 4(b), red line. For this example ($R = 20$, $\alpha = 4.9$), the binned data shows that cells in regions of most negative order experience a slightly higher magnitude of parallel stress compared to cells in high-order regions. The average order at each aspect ratio and curvature is shown in supplementary information Fig. S6(c,f).

This trend appears much more robustly in data aggregated across multiple simulations with the same cell aspect ratio or surface curvature. Plots of normalized parallel stress binned by order and averaged across all simulations with the same aspect ratio or curvature are shown in Fig. 4(c) and 4(d), respectively. For all cases, the average normalized stress decreases with increasing orientational order. Specifically, in regions of high orientational order ($S > 0.5$), the local average of normalized stress approaches unity, or $\sigma_{\parallel} \approx \langle\sigma_{\parallel}\rangle$. In regions of negative orientational order, however, the local average of normalized stress is 15% to 22% larger than the global average stress, or $\sigma_{\parallel} \geq 1.15\langle\sigma_{\parallel}\rangle$. The same analysis was also performed for the perpendicular component of stress and no consistent relation was observed in this case, shown in supplementary information Fig. S7.

The stress in other active nematics, such as those composed of epithelial cells, is higher near $+1/2$ topological defects, which themselves are low-order regions by definition [16]. To investigate whether this effect was responsible for the correlation of high stress and low order in bacterial monolayers, stress near topological defects was compared to the previously calculated stress in the most negative order regions ($S < 0.1$). The mean value of the parallel component of the Virial stress ($\sigma_{\parallel}$) was computed for all cells within close proximity ($r = l_0/2$) of a $\pm 1/2$ topological defect within the monolayer. Then, this value was compared to the average normalized parallel stress of the bin with the lowest orientational order and is shown in Fig. 4(e). For all cases, the average deviation from the mean stress near $\pm 1/2$ defects is less than 5%, or $\sigma_{\parallel} \leq 1.05\langle\sigma_{\parallel}\rangle$. The average order in the same regions near these defects is between $0.2 < S < 0.5$, shown in the supplementary information Fig. S8. In contrast, the average deviation from the mean stress in regions of negative orientational order is always greater than 15%, or $\sigma_{\parallel} \geq 1.15\langle\sigma_{\parallel}\rangle$, for all cell aspect ratios and substrate curvatures. This shows that the observed high stress-low order correlation in this system is

not caused by stress concentration near topological defects, and is instead a distinct effect.

IV. DISCUSSION

Previous work on monolayers of growing hard-rod cells has shown that, in the case of a solid-liquid growth substrate, the overdamped Hertzian model described here accurately models the system [2]. We have shown through comparisons of simulations and experiments that this model can be extended to a liquid-liquid interface. To do this, we modeled the surface tension forces fixing cells to the interface with the constraint that cells lie with their center on the interface and their orientation parallel to the local tangent plane. This constraint matches behavior seen in experiments on cells adsorbed at liquid-liquid interfaces, both in this work (i.e. shown in Fig. 1(a)) and elsewhere [26]. The liquid-liquid extension holds as long as the curvature is small compared to the cell length, so the interface is locally flat, and the packing fraction is small enough to prevent inter-cell forces from affecting the interface shape. Deformations of the interface occur after the point of complete interface coverage [25, 26]. The equations of motion in the liquid-liquid version remain overdamped because of the hydrodynamic drag on the nonmotile cells.

Application of this model to flat monolayers has shown that microdomain size increases with increasing cell aspect ratio [2]. Our work is consistent with this result, and further confirms that the trend holds for monolayers growing on curved surfaces as well. Additionally, while previous work demonstrated the relation between microdomain size and aspect ratio for an unconfined growing colony [2], our results show that the same relation is true for a growing colony confined to a finite substrate area, such as the surface of a sphere. Together, these show that microdomain formation and its dependence on cell aspect ratio are robust collective behaviors in growing hard-rod monolayers under a variety of conditions.

We find a new dependence of microdomain area on the curvature of the surface. Regardless of cell aspect ratio, higher curvature substrates resulted in smaller microdomains. This decrease in alignment is attributable to the structure of microdomains, which consist primarily of near-parallel lines of cells spaced one cell width apart in both flat [2] and curved systems. The "straightest" lines possible on the surface of a sphere are great circles, which cannot lie parallel to each other. Thus, as domain size increases, the lines of cells must either converge or bend, deviating from the great circle. In either case, this prevents the

microdomain from forming a fully parallel crystalline structure, decreasing its stability and leading to fracture. On more curved surfaces these lines of cells diverge at shorter length scales, leading to lower average microdomain sizes, while less curved surfaces will eventually limit to the flat case in which microdomain size is limited only by growth-powered activity [2]. With the growth rate and range of curvatures simulated here, both activity and curvature play a role in inhibiting microdomain size with neither effect dominating, and therefore microdomain size does not exhibit a straightforward dependence on curvature. Such dependence could be investigated by simulating higher-curvature surfaces or much lower growth rates.

We also find that the extensile (parallel) stress of the monolayer has the highest magnitude in cells with negative local order. This is a contrast to previous simulations of bacteria growing in a channel with outlets on the ends, where stress could be released as cells exited the system [28]. In these systems, lower-order regions were found to have lower stress, the opposite of our findings. The likely source of this difference is the fact that our system has no way to reduce total stress other than the reorientation of cells to more efficient packing.

More recent simulations of a similar setup have produced a model for stress distribution in highly-aligned columns of cells, where the parallel and perpendicular components of stress decouple [31]. While our system is much more confined, the columnar model still sheds light on the stress behavior of high-order cells in microdomains compared to that of low-order cells. Columns of high-order cells compressed at both ends can distribute extensional stress evenly throughout the column, while disordered cells have no way to distribute their stress without reorganizing their local geometry. This could lead to greater stress buildup in individual disordered cells.

Our results are robust for a range of packing fractions. While the results presented here are specifically for $\phi = 1.05$, the same analysis addressing the curvature-microdomain area and order-stress relationships for $\phi = 1.1$ can be found in the supplementary information Fig. S9 and Fig. S10, respectively. This analysis shows that both relations persist in the same form at the higher packing fraction. For packing fractions $\phi < 1.05$, the surface is not homogeneously covered, and we would expect results to differ significantly.

In a continuous (non-granular) active nematic composed of flexible epithelial cells, extensile stress is highest at positively charged topological defects [16]. These stress concentrations cause the cell layer to deform at these points, producing mounds localized near the defects

[16]. Similar deformations are seen in other continuous active nematics at deformable 2D interfaces, such as microtubules on the surface of a vesicle or actin fibers in the morphogenesis of multicellular organisms [32, 33], and this behavior has been further confirmed and studied in numerous simulations and theoretical works [34–39]. In a granular active nematic, our simulations show that extensile stress concentrates at all negative-order cells rather than at the locations of point +1/2 topological defects, likely because the non-continuous nature of the director field decreases the robustness of defect definitions. This can be expected to result in different forms of deformation under growth stress. In fact, comparable deformations have been imaged in systems of *A. borkumensis* growing on the surface of oil droplets in water [25, 26]. As confocal images in these experiments show that cells maintain the same surface attachment during deformations, a similar simulation setup to ours in which the interface's shape is allowed to change and respond to cell growth and forces could be an effective way to model these deformations.

Our results are relevant for systems of bacteria growing at liquid-liquid interfaces, such as at the oil-water interface of a droplet. For example, previous work has shown that cell growth confined to the surface of a droplet produces tube-like protrusions similar to those produced by continuous active nematics [25, 26]. However, a complete theoretical description of droplet deformation by cell growth is still lacking. Our results suggest that these protrusions should nucleate at lower-order sites such as boundaries between microdomains, rather than nucleating exclusively at +1/2 defects. By extension, this allows us to predict how interfacial curvature influences deformations due to the underlying microstructure. For example, higher curvature (small radii) droplets will produce more closely spaced protrusions since the characteristic size of their microdomains decreases.

Our results also emphasize the importance of constituent particle properties on collective behavior.

While a hard-rod monolayer exhibits many of the same properties as a nematic composed of microtubules or other flexible components [11], it produces microdomains that are distinct from the continuous alignment fields of other active nematic systems. Furthermore, its internal forces are not well predicted by topological defects, which are themselves less robustly defined due to the non-continuous alignment field. Other fundamental differences between granular and continuous nematics in more highly aligned systems have recently been discovered as well [31]. The partially granular nature of a bacterial monolayer is clearly of

great importance to understanding its collective behavior.

In conclusion, we have shown that stress distributions in a hard-rod bacterial monolayer vary predictably based on cell aspect ratio and substrate curvature. Specifically, our simulations show that stress in a hard-rod monolayer concentrates in negative-order cells, which occur at the boundaries of microdomains. The length scale of these microdomains increases with cell aspect ratio and decreases with substrate curvature. These results demonstrate that while a bacterial monolayer can be effectively modeled as a continuum active nematic, in some cases when its cells act as hard rods, the alignment and stress distributions behave in distinctly different ways.

V. AUTHOR CONTRIBUTIONS

Blake Langeslay: Conceptualization, Methodology, Software, Investigation, Formal analysis, Visualization, Writing - original draft, Writing - review and editing. **Gabriel Juarez:** Conceptualization, Methodology, Supervision, Writing - original draft, Writing - review and editing.

VI. CONFLICTS OF INTEREST

There are no conflicts of interest to declare.

VII. ACKNOWLEDGEMENTS

This work used the eXtreme Science and Engineering Discovery Environment (XSEDE), which is supported by National Science Foundation grant number #ACI-1548562. In particular, we used the Pittsburgh Supercomputing Center's Bridges-2 resources under allocation ID PHY210132. We thank Vincent Hickl for assistance with experiments on growing bacterial monolayers at liquid interfaces.

[1] A. Persat, C. Nadell, M. Kim, F. Ingremeau, A. Siryaporn, K. Drescher, N. Wingreen, B. Bassler, Z. Gitai and H. Stone, *Cell*, 2015, **161**, 988–997.

[2] Z. You, D. J. G. Pearce, A. Sengupta and L. Giomi, *Phys. Rev. X*, 2018, **8**, 031065.

[3] M.-C. Duvernoy, T. Mora, M. Ardré, V. Croquette, D. Bensimon, C. Quilliet, J.-M. Ghigo, M. Balland, C. Beloin, S. Lecuyer and N. Desprat, *Nature Communications*, 2018, **9**, 1120.

[4] D. Boyer, W. Mather, O. Mondragón-Palomino, S. Orozco-Fuentes, T. Danino, J. Hasty and L. S. Tsimring, *Physical Biology*, 2011, **8**, 026008.

[5] M. A. A. Grant, B. Wacław, R. J. Allen and P. Cicuta, *Journal of The Royal Society Interface*, 2014, **11**, 20140400.

[6] D. Volfson, S. Cookson, J. Hasty and L. S. Tsimring, *Proceedings of the National Academy of Sciences*, 2008, **105**, 15346–15351.

[7] K. Marshall, *Advances in Colloid and Interface Science*, 1986, **25**, 59–86.

[8] M. Krajnc, P. Stefanic, R. Kostanjšek, I. Mandic-Mulec, I. Dogsa and D. Stopar, *npj Biofilms and Microbiomes*, 2022, **8**, 25.

[9] J. C. Conrad, *Journal of Industrial Microbiology and Biotechnology*, 2020, **47**, 725–738.

[10] T. H. R. Niepa, L. Vaccari, R. L. Leheny, M. Goulian, D. Lee and K. J. Stebe, *Scientific Reports*, 2017, **7**, 17864.

[11] D. Dell'Arciprete, M. L. Blow, A. T. Brown, F. D. C. Farrell, J. S. Lintuvuori, A. F. McVey, D. Marenduzzo and W. C. K. Poon, *Nature Communications*, 2018, **9**, 4190.

[12] K. Copenhagen, R. Alert, N. S. Wingreen and J. W. Shaevitz, *Nature Physics*, 2021, **17**, 211–215.

[13] Y. I. Yaman, E. Demir, R. Vetter and A. Kocabas, *Nature Communications*, 2019, **10**, 2285.

[14] L. Giomi, M. J. Bowick, X. Ma and M. C. Marchetti, *Phys. Rev. Lett.*, 2013, **110**, 228101.

[15] S. P. Thampi, R. Golestanian and J. M. Yeomans, *Phys. Rev. Lett.*, 2013, **111**, 118101.

[16] P. Guillamat, C. Blanch-Mercader, G. Pernollet, K. Kruse and A. Roux, *Nature Materials*, 2022, **21**, 588–597.

[17] T. B. Saw, A. Doostmohammadi, V. Nier, L. Kocgozlu, S. Thampi, Y. Toyama, P. Marcq, C. T. Lim, J. M. Yeomans and B. Ladoux, *Nature*, 2017, **544**, 212–216.

[18] K. D. Endresen, M. Kim, M. Pittman, Y. Chen and F. Serra, *Soft Matter*, 2021, **17**, 5878–5887.

[19] T. Turiv, J. Krieger, G. Babakhanova, H. Yu, S. V. Shiyanovskii, Q.-H. Wei, M.-H. Kim and O. D. Lavrentovich, *Science Advances*, 2020, **6**, eaaz6485.

[20] K. Kawaguchi, R. Kageyama and M. Sano, *Nature*, 2017, **545**, 327–331.

[21] Z. You, D. J. G. Pearce and L. Giomi, *Science Advances*, 2021, **7**, eabc8685.

[22] F. Alaimo, C. Köhler and A. Voigt, *Scientific Reports*, 2017, **7**, 5211.

[23] P. W. Ellis, D. J. G. Pearce, Y.-W. Chang, G. Goldsztein, L. Giomi and A. Fernandez-Nieves, *Nature Physics*, 2018, **14**, 85–90.

[24] M. Nestler and A. Voigt, *Communications in Computational Physics*, 2022, **31**, 947–965.

[25] V. Hickl and G. Juarez, *Soft Matter*, 2022, **18**, 7217–7228.

[26] M. Prasad, N. Obana, S.-Z. Lin, K. Sakai, C. Blanch-Mercader, J. Prost, N. Nomura, J.-F. Rupprecht, J. Fattaccioli and A. S. Utada, *bioRxiv*, 2022.

[27] C. W. Wolgemuth, *Biophysical Journal*, 2008, **95**, 1564–1574.

[28] S. Orozco-Fuentes and D. Boyer, *Phys. Rev. E*, 2013, **88**, 012715.

[29] H. Hertz, *On the Contact of Rigid Elastic Solids and on Hardness*, MacMillan, 1882.

[30] S. J. DeCamp, G. S. Redner, A. Baskaran, M. F. Hagan and Z. Dogic, *Nature Materials*, 2015, **14**, 1110–1115.

[31] J. Isensee, L. Hupe, R. Golestanian and P. Bittihn, *Journal of The Royal Society Interface*, 2022, **19**, 20220512.

[32] F. C. Keber, E. Loiseau, T. Sanchez, S. J. DeCamp, L. Giomi, M. J. Bowick, M. C. Marchetti, Z. Dogic and A. R. Bausch, *Science*, 2014, **345**, 1135–1139.

[33] Y. Maroudas-Sacks, L. Garion, L. Shani-Zerbib, A. Livshits, E. Braun and K. Keren, *Nature Physics*, 2021, **17**, 251–259.

[34] L. Metselaar, J. M. Yeomans and A. Doostmohammadi, *Phys. Rev. Lett.*, 2019, **123**, 208001.

[35] L. J. Ruske and J. M. Yeomans, *Phys. Rev. X*, 2021, **11**, 021001.

[36] J. A. Santiago, *Phys. Rev. E*, 2018, **97**, 052706.

[37] F. Vafa and L. Mahadevan, *Physical Review Letters*, 2008, **129**, 098102.

[38] L. A. Hoffmann, L. N. Carenza, J. Eckert and L. Giomi, *Science Advances*, 2022, **8**, eabk2712.

[39] R. Alert, *Journal of Physics A: Mathematical and Theoretical*, 2022, **55**, 234009.